GDCh

Research Articles

Angewandte
Chemie
International Edition
www.angewandte.org

VIP | Solid-State Batteries | *Very Important Paper*

Time-Temperature-Transformation (TTT) Diagram of Battery-Grade Li-Garnet Electrolytes for Low-Temperature Sustainable Synthesis

Yuntong Zhu, Michael Chon, Carl V. Thompson, and Jennifer L. M. Rupp*

Abstract: Efficient and affordable synthesis of Li$^+$ functional ceramics is crucial for the scalable production of solid electrolytes for batteries. Li-garnet Li$_7$La$_3$Zr$_2$O$_{12-d}$ (LLZO), especially its cubic phase (cLLZO), attracts attention due to its high Li$^+$ conductivity and wide electrochemical stability window. However, high sintering temperatures raise concerns about the cathode interface stability, production costs, and energy consumption for scalable manufacture. We show an alternative "sinter-free" route to stabilize cLLZO as films at half of its sinter temperature. Specifically, we establish a time-temperature-transformation (TTT) diagram which captures the amorphous-to-crystalline LLZO transformation based on crystallization enthalpy analysis and confirm stabilization of thin-film cLLZO at record low temperatures of 500 °C. Our findings pave the way for low-temperature processing via TTT diagrams, which can be used for battery cell design targeting reduced carbon footprints in manufacturing.

[*] Y. Zhu, M. Chon, C. V. Thompson, J. L. M. Rupp
Department of Materials Science and Engineering, Massachusetts Institute of Technology, Cambridge, MA 02139 (USA)
E-mail: jrupp@mit.edu

J. L. M. Rupp
Department of Chemistry, Technical University Munich, Garching 85748 (Germany)

J. L. M. Rupp
TUMint. Energy Research GmbH, Lichtenbergstr. 4, Garching 85747 (Germany)

J. L. M. Rupp
Department of Electrical and Computer Engineering, Technical University Munich, 80333 Munich (Germany)
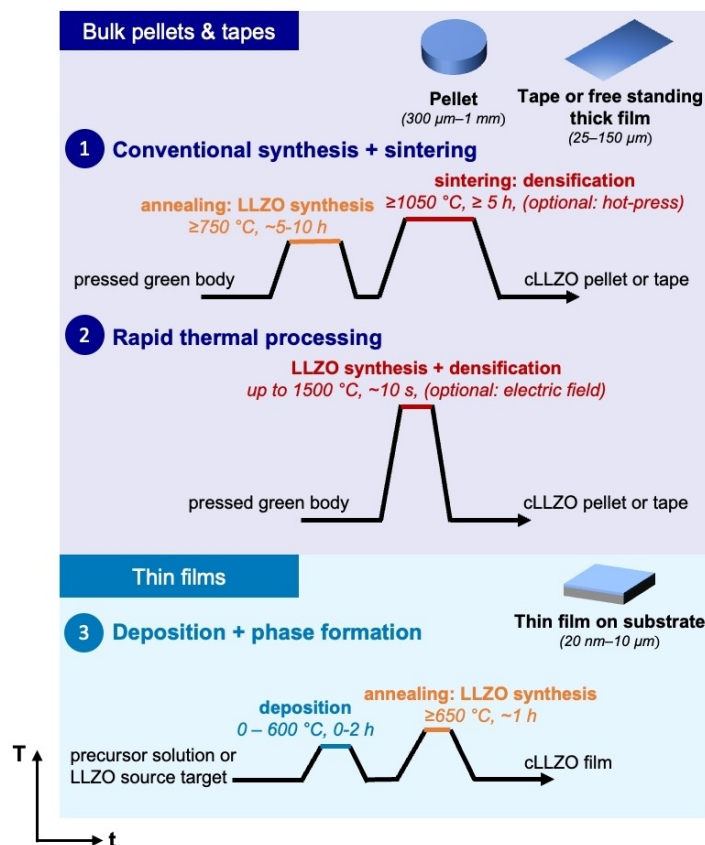
J. L. M. Rupp
Department of Electrical Engineering and Computer Science, Massachusetts Institute of Technology, Cambridge, MA 02139 (USA)

Introduction

Battery performance and costs are the two most important factors when evaluating specific cell design and cell chemistry for use in electric vehicles (EVs).[1–4] The former largely determines the driving distance and lifetime of EVs, whereas the latter dictates the cost-competitiveness of EVs relative to internal combustion vehicles (ICVs).[2,3] To date, Li-ion batteries have shown promise as the most reliable energy-storage solution for EVs owing to their improved energy density and cycle life compared with that of battery systems developed earlier (e.g., lead-acid batteries, nickel-cadmium batteries). State-of-the-art Li-ion batteries with graphite (or graphite/Si composite) anodes, LiNiMnCoO$_{2-d}$ (NMC) or LiNiCoAlO$_{2-d}$ (NCA) cathodes, and organic liquid electrolytes are able to achieve gravimetric energy densities of 250–300 Wh kg^{-1} at the cell level,[2] associated with a cost of approximately US$100 kWh^{-1}.[5] To accelerate the transition from ICVs to EVs, the US Department of Energy (DOE) set long-term objectives of reaching a production cost of < US$60 kWh^{-1} at the cell level and a specific energy density of > 500 Wh kg^{-1} at the battery level by 2030.[6] One promising approach to achieve these ambitious goals is to revive the use of a Li-metal anode in an all-solid-state or hybrid battery configuration with partial or full substitution of the state-of-the-art organic liquid electrolytes and polymer separators by thin ceramic solid-electrolyte separators to achieve high energy density while minimizing the risk of Li dendrite growth and thermal runaway.[1,7] The ideal solid-electrolyte separators should possess high Li-ion conductivity over a wide temperature range and good electrochemical and chemical stability against both a Li-metal anode and high-voltage oxide cathode.[1,7,8] In addition, the electrolyte materials should be mechanically robust (i.e., exhibit high fracture toughness) against Li-dendrite propagation.[1,9–12] State-of-the-art ceramic solid electrolytes can be classified into two types based on their chemical composition, namely, oxides and sulfides.[7] Sulfide-based electrolytes, including argyrodite-type Li$_6$PS$_5$X (X=Cl, Br, I)[13,14] and Li$_2$S-P$_2$S$_5$ glasses,[15] possess limited electrochemical stability windows (< 1 V)[16–18] and poor air stability, restricting their energy density, scale-up processibility, and safety toward application in battery cells.[7] Comparatively, oxide-based electrolytes offer wider electrochemical stability windows and higher fracture toughness and require a less constrained atmosphere for processing.[1,7,18–20]

Among the widely studied oxide electrolytes, garnet-type Li$_7$La$_3$Zr$_2$O$_{12-d}$ (LLZO) has demonstrated electro-

chemical stability between 0 and 6 V,[1,21] enabling direct and stable pairing with high-voltage cathodes and Li-metal anodes, making this material an attractive option for use in high-energy-density all-solid-state or hybrid batteries. To date, LLZO electrolytes can be processed either as bulk pellets or tapes with thicknesses generally >25 μm (tapes $<100\,\mu$m can be brittle and difficult to handle)[22,23] or as thin films with thicknesses between 0.2 and 10 μm (Fig-ure 1a).[1,8,24] Depending on the form and desired thickness of LLZO, either sintering (>1050 °C for pellets or tapes)[21,25–33] or annealing (>650 °C for films)[8,24,34–38] are required to synthesize LLZO in its highly conductive cubic phase (Figure 1b), see Ref. [39] for high-statistics data mining on sintering. An additional summary of the bulk and thin-film LLZO synthesis is presented in Table S1.
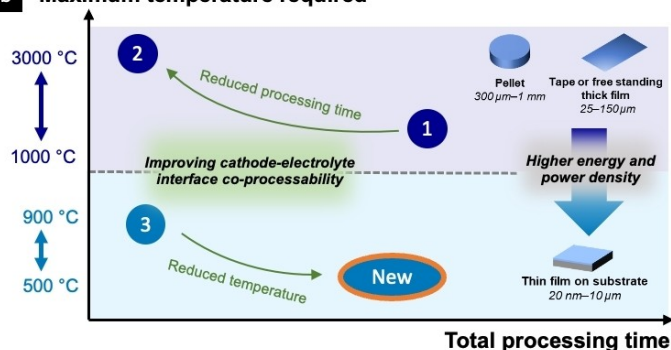

Figure 1. (a) Annealing and sintering steps to achieve cubic-phase LLZO under three different processing routes, including conventional synthesis + sintering and rapid thermal processing for bulk pellet and tape processing, and deposition + phase formation for thin-film processing. (b) Schematic illustration of the state-of-the-art maximum processing temperature vs. processing time. Reducing the processing temperature or time are both viable and preferred routes to improve the cathode-electrolyte interface co-processability and reduce reactions at interfaces. The energy and power density of a solid-state battery can be improved by reducing the solid-electrolyte thickness (shifting from ceramic pellets or tapes to thin films).

From a cell-integration perspective, these LLZO pellets, tapes, or films need to be co-processed with high-voltage oxide-based cathodes (e.g., NMC, NCA) to achieve good mechanical bonding and low interfacial resistance at the LLZO-cathode interface.[25] However, prior studies have shown that oxide-based cathodes can be irreversibly reduced or decomposed into low-capacity phases at a co-processing temperature above 600 °C,[25,40] which is clearly lower than the classic sintering temperatures for pellet and tape-type LLZO and therefore lead to a reduced total capacity for the cathodes. Thus, the commercialization of oxide-electrolyte-based solid-state batteries necessitates a complete rethinking and redesign of electrolyte separator processing as well as the cell-integration routes, preferably at lowered co-sintering or co-annealing temperatures. Importantly, newly defined processing routes should ensure chemical stability at cathode-electrolyte interfaces and show promise toward achieving the DOE cost projection of $< \mathrm{US\$60\ kWh^{-1}}$.[6,41]

From a second perspective, low-temperature processing is favorable for next-generation $\mathrm{Li^+}$ ceramic electrolytes as it can significantly reduce manufacturing costs by lowering the energy input. An earlier cost analysis suggested that the high-temperature annealing and sintering steps account for approximately 75 % of the total production cost for $\mathrm{Li^+}$ solid electrolytes.[1] This cost can make up an even higher fraction of the production cost when there is a spike in energy prices. For instance, the 2022 rise in energy costs led to temporary challenges for the energy-intensive ceramic and glass industries. It is now critical for the industry to re-examine the state-of-the-art processing routes and point toward a future where achieving greater energy efficiencies in production is a top priority. Specifically, any option to achieve similar structure and functionality for a $\mathrm{Li^+}$ ceramic (or glass) electrolyte at lowered processing temperatures without sintering steps is of utmost importance for future sustainable and low-cost electrolyte and solid-state battery production. Alternative sinter-free processing routes stemming from the direct "liquid-to-solid" densification of $\mathrm{Li^+}$ electrolytes at low temperatures are promising options to be explored. Additionally, these direct densification routes do not require ceramic powder processing, which is beneficial in reducing the cost and energy consumption associated with the production of ceramic $\mathrm{Li^+}$ electrolytes. However, to date, only a few academic works have explored the direct "liquid-to-solid" densification routes for battery-grade $\mathrm{Li^+}$ ceramic electrolyte processing, see Ref. [8] and[42] for studies on the sequential decomposition synthesis (SDS) of LLZO. Despite being a timely and relevant process, an annealing temperature of 750 °C is still required to achieve the highly conductive cLLZO via SDS, which can still be too high for LLZO-cathode co-processing. Lower-temperature processing options have yet to be explored.

In this work, we explore alternative synthesis conditions for direct crystallization using "liquid-to-solid" SDS-processed LLZO electrolytes at reduced temperatures through the establishment of the first time-temperature-transformation (TTT) diagram. To enable rational design of the low-temperature routes, we first obtain a fundamental understanding of the kinetics of the phase transformation from amorphous LLZO (aLLZO) to crystalline cLLZO through Raman spectroscopy and differential scanning calorimetry (DSC).[43] A common approach to understand and modulate the phase-transformation kinetics of a glass-ceramic or metallic glass is through the construction of a TTT diagram,[44–47] a 2D representation plot of the temperature and time at which a material undergoes a phase transformation.[46,48] Specifically, we deconvoluted the crystallization process of SDS-processed thin-film LLZO into three unique steps and constructed the very first TTT diagram for thin-film LLZO based on the analysis of crystallization enthalpies. From there, we designed three alternative low-temperature processing routes and confirmed the successful synthesis of thin-film cLLZO at temperatures as low as 500 °C.[49] Fundamentally, we demonstrate the establishment and use of a TTT diagram in analyzing the phase-transition and crystallization kinetics of thin-film LLZO and designing alternative ceramic film processing routes. Technologically, we see the promise of the newly proposed low-temperature processing routes to benefit the materials integration and manufacturing scale-up at a reduced cost for LLZO-based solid-state batteries and beyond.

Results and Discussion

Synthesis and phase evolution from aLLZO to crystalline cLLZO

Figure 2a displays surface and cross-sectional scanning electron microscopy (SEM) images of the as-deposited Al-doped $\mathrm{Li_7La_3Zr_2O_{12}}$ (LLZO) film prepared by the SDS method (see Ref. [8] for more details about this low-cost "liquid-to-solid" direct densification method that allows the direct formation of ceramic films without powder processing). The film exhibits an even and full surface coverage on the MgO substrate with a thickness of 3.0 ± 0.8 μm. Raman spectroscopy provides insights into the LLZO phase evolution and crystallization. Figure 2b displays the Raman spectra of the 300 °C as-deposited film and the 520 °C, 620 °C, and 750 °C post-annealed films (isothermal time = 15 min), along with reference spectra of cubic $\mathrm{Li_7La_3Zr_2O_{12}}$, tetragonal $\mathrm{Li_7La_3Zr_2O_{12}}$, pyrochlore $\mathrm{La_2Zr_2O_7}$, and $\mathrm{LiNO_3}$, the original Li salt used in SDS processing.

For the *as-deposited film*, we observed a general amorphous nature of the film with peaks developed from the undecomposed $\mathrm{LiNO_3}$ precursor salt. Specifically, a broad Raman signal was detected for wavenumbers between 300 and 700 $\mathrm{cm^{-1}}$ with no appearance of the O–Li–O vibrational band ($\mathrm{E_g}$ and $\mathrm{T_{2g}}$) or O–Zr–O stretching band ($\mathrm{A_{1g}}$), suggesting a highly disordered amorphous structure with only short-range order. Outside of the 300–700 $\mathrm{cm^{-1}}$ wavenumber range, the two predominant peaks at 240 and 738 $\mathrm{cm^{-1}}$ and two minor peaks at 100 and 131 $\mathrm{cm^{-1}}$ indicate the presence of undecomposed $\mathrm{LiNO_3}$ precursor salt. At 750 °C, we observed a fully crystallized cLLZO film, in agreement with the previously reported crystallization temperature from in situ transmission electron microscopy (TEM) and in situ Raman spectroscopy.[42] Specifically, the
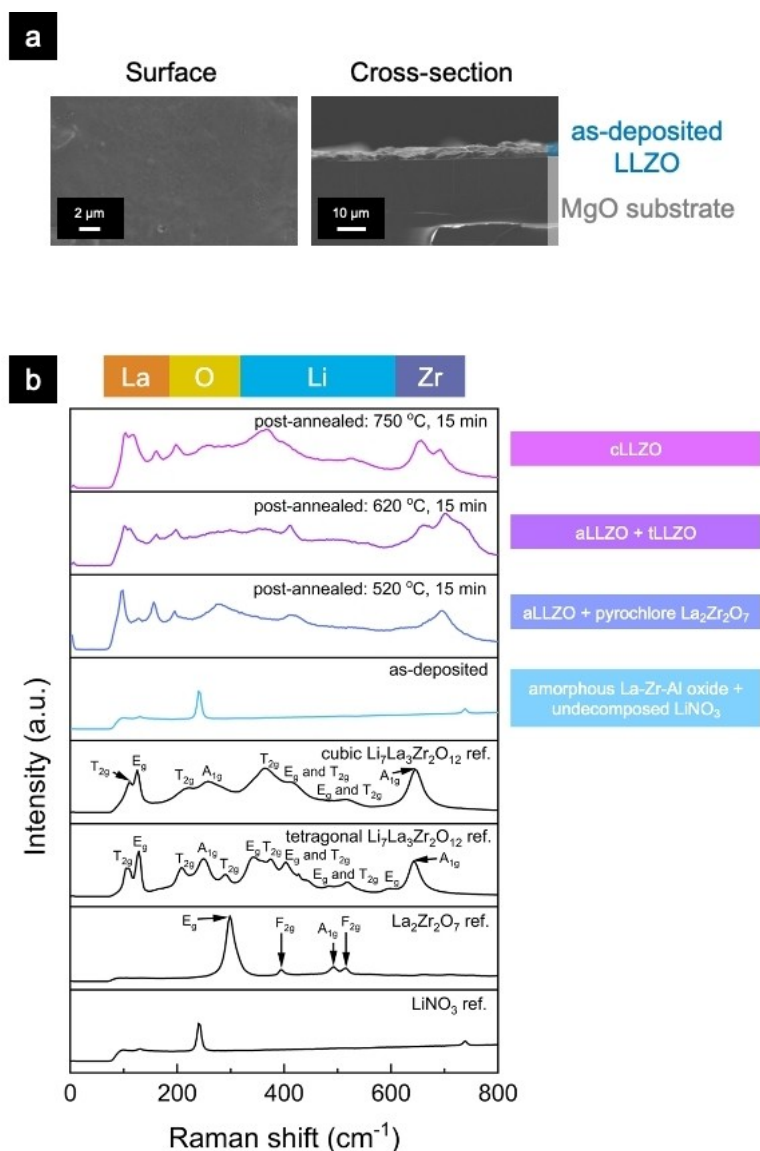
Figure 2. (a) Surface and cross-sectional SEM images of a 300 °C as-deposited LLZO film. The film exhibits full surface coverage with a thickness of 3.0 ± 0.8 μm. (b) Raman spectra of the as-deposited LLZO film, and the 520 °C, 620 °C, and 750 °C post-annealed LLZO films. Additional reference spectra of $LiNO_3$, $La_2Zr_2O_7$, tetragonal $Li_7La_3Zr_2O_{12}$, cubic $Li_7La_3Zr_2O_{12}$ are displayed in black.

two intense peaks at 105 and 116 cm^{-1} were identified as the T_{2g} and E_g modes of O–La–O vibration, and the two peaks centered at 655 and 691 cm^{-1} were assigned to the O–Zr–O stretching band (A_{1g} mode).[50,51] The peak divergence of the O–Zr–O stretching band may be defect-related, which causes deviation of the local symmetry and introduces anisotropic strains to the lattice (similar effects have been reported in metal-oxide thin films, including doped CeO_2 films in Ref. [52,53]). Alternatively, the peak divergence may be correlated to the co-existence of more than one LLZO cubic phase, i.e., 220 (*I-43d*) and 230 (*Ia-3d*) space-group cubic phases. These phases have different Li coordination sites and symmetries,[12] which may lead to the local structure deviation in ZrO_6 octahedra. Other cLLZO phase characteristics include the peak centered at 255 cm^{-1}, corresponding to the oxygen-bending band of T_{2g} and A_{1g},[50]

and the peaks centered at 368 and 527 cm^{-1}, assigned to the O–Li–O vibration bands (T_{2g} and E_g/T_{2g} mode) in LiO_6 octahedra.[51]

We next analyzed the local structure evolution between 300 °C and 750 °C based on the Raman spectra displayed in Figure 2b. Upon heating to 520 °C, the film was composed of aLLZO with the additional presence of pyrochlore $La_2Zr_2O_7$ nuclei. Specifically, the prominent peaks observed at 96 and 127 cm^{-1} (T_{2g} mode) signify the O–La–O vibration in aLLZO, and the broad peaks at 415 and 697 cm^{-1} can be correlated to the E_g and T_{2g} modes of O–Li–O vibration[51] and the A_{1g} mode of O–Zr–O stretching in aLLZO,[50,51] respectively. In addition, the peak centered at 279 cm^{-1} is attributed to the E_g mode of ZrO_6 bending in pyrochlore $La_2Zr_2O_7$.[54,55] This result is consistent with the earlier reported in situ TEM and in situ X-ray diffraction (XRD)

results in Ref. [8,42], where $La_2Zr_2O_7$ nuclei appear as an intermediate phase during LLZO crystallization. Crystallization progressed with diminishing of the pyrochlore $La_2Zr_2O_7$ local ordering and the ongoing formation of tetragonal LLZO (tLLZO) local ordering as we further increased the film annealing temperature to 620°C. The peak at 279 cm^{-1} (E_g mode of ZrO_6 bending from pyrochlore $La_2Zr_2O_7$) disappeared, and three broad peaks emerged at 296, 361, and 410 cm^{-1}, corresponding to the A_{1g} mode of oxygen bending, E_g mode of O–Li–O vibration, and T_{2g} mode of O–Li–O vibration in tLLZO,[51] respectively. These results also agree with earlier reported in situ TEM results (see Ref. [42] for more evidence), where tLLZO nuclei emerged through Li diffusion from aLLZO to the prior formed $La_2Zr_2O_7$ nuclei.[42] We also observed minor peaks at 155 and 196 cm^{-1} in all the spectra, attributable to the rotatory and translator motion of CO_3^{2-} from the surface chemistry variation of Li_2CO_3,[56,57] which may be formed from the direct contact of films with moisture in the air during sample transfer and spectrum collection.

We hereby confirm by Raman spectroscopy the formation of cLLZO at 750°C for a heating rate of 5°C min^{-1} through multi-step nucleation and phase evolution from the original aLLZO phase. Specifically, the 1st step involves the formation of pyrochlore $La_2Zr_2O_7$ nuclei in the predominate aLLZO structure, as evidenced by the 520°C post-annealed aLLZO spectra. Upon further increasing the temperature to 620°C, the formation of tLLZO through lithiation of $La_2Zr_2O_7$ nuclei was confirmed, which we denoted as the 2nd crystallization step. The 3rd crystallization step starts off at a temperature above 620°C with the transformation from aLLZO and tLLZO to cLLZO. As suggested by earlier LLZO structure studies, see Ref. [58], this step involves Li local reordering in the occupied sites within the crystalline tLLZO structure, which transforms tLLZO (with regular and fully occupied Li sites) into cLLZO (with disordered Li site occupation). We next employed DSC to further investigate the kinetics of the phase transformation from aLLZO to crystalline cLLZO.

Deconvolution of crystallization kinetics from aLLZO to crystalline cLLZO

DSC measurements were performed at different heating rates (i.e., 5 to 20°C min^{-1}) to characterize the kinetics and enthalpy changes during the crystallization from aLLZO to cLLZO. This analysis forms the basis for constructing the first TTT diagram to enable precise phase definitions and to guide future LLZO low-temperature processing. Four important peaks were observed for each of the DSC measurements, as displayed in Figure 3, including an exothermic peak at ≈341–450°C and three endothermic peaks at ≈243–277°C, ≈490–663°C, and ≈667–710°C. The two endothermic DSC peaks at ≈490–663°C and ≈667–710°C in Figure 3 can be correlated to the crystallization of LLZO according to the phase evolution depicted in the Raman spectra in Figure 2b, where fully crystallized cLLZO is detected after annealing at 750°C. In addition, our

previous study on aLLZO suggested that the crystallization of LLZO occurs between 490 and 720°C (see TEM and in situ Raman analyses in Ref. [42] for more details), which is consistent with the DSC observation in this work. Prior to the crystallization, the endothermic peak at ≈243–277°C can be assigned to the melting of $LiNO_3$, the Li precursor salt typically used in SDS processing, during which the deposited LLZO sample intakes heat and leads to a solid-to-liquid phase transformation for $LiNO_3$.[59] Furthermore, the exothermic peaks at ≈341–450°C can be related to the decomposition of $LiNO_3$ (see detailed analysis in Figure 2g of Ref. [8]).

To better understand the kinetics of the observed crystallization peaks (i.e., the peaks at 490–663°C and 667–710°C), we next performed peak deconvolution and fitting and obtained phase-transformation peak temperatures (T_p) and phase-transformation enthalpy changes (ΔH). We show an example of a DSC scan measured at a heating rate of 10°C min^{-1} in Figure 4a, where the first and second endothermic peaks sit between 492–639°C and 667–710°C, respectively, representing the crystallization of SDS-processed LLZO. The asymmetric shape of the first crystallization peak with a left-skewed tail (evidenced by different slopes) suggested a sequence of two chemical and structural transformation processes and was fitted to two sub-peaks, including the lower-temperature sub-peak fitted in violet at 492–627°C and the higher-temperature one fitted in lavender blue at 547–639°C in Figure 4a. The lower-temperature sub-peak is associated with the 1st crystallization step of pyrochlore $La_2Zr_2O_7$ nuclei formation illustrated in Figure 4b, as evidenced by the analysis of the Raman spectra in Figure 2b and the in situ TEM results in Ref. [42]. Furthermore, the Raman spectra indicate the emergence of tLLZO when the annealing temperature increases above 620°C, suggesting that the higher-temperature sub-peak may be related to the 2nd crystallization step of lithiation and transformation from pyrochlore $La_2Zr_2O_7$ to tLLZO nuclei, depicted in Figure 4b. Unlike the first DSC peak, the second DSC peak (T_{p2}: 667–710°C) in Figure 4a has a symmetric shape and can be fitted into a single peak centered at 689°C. The fitted peak overlaps with the temperatures at which the formation of cLLZO was observed in the Raman spectra, see Figure 2b, and is therefore assigned as the 3rd crystallization step. We present further details on the DSC peak fittings in Figure S1a–c and discussed the variation in the crystallization peak temperatures, i.e., T_{p1}, T_{p2}, and T_{p3}, and their corresponding crystallization enthalpies, i.e., ΔH_1, ΔH_2, and ΔH_3 in Figure S2a and b (also see data in Table S2).

We next developed the progress of the crystallization plot in Figure 4c based on the three crystallization steps deconvolved in Figure 4a. Different from classical glass-ceramic or metallic glass TTT diagrams, where the cooling curves are determined for the transformation from the undercooled liquid to the crystalline state, the LLZO films crystallize upon heating to temperatures higher than the SDS deposition temperatures.[46] The progress of phase transformation from aLLZO to biphasic aLLZO + $La_2r_2O_7$ nuclei and tLLZO nuclei and finally to fully crystallized cLLZO at different temperatures was calculated by dividing
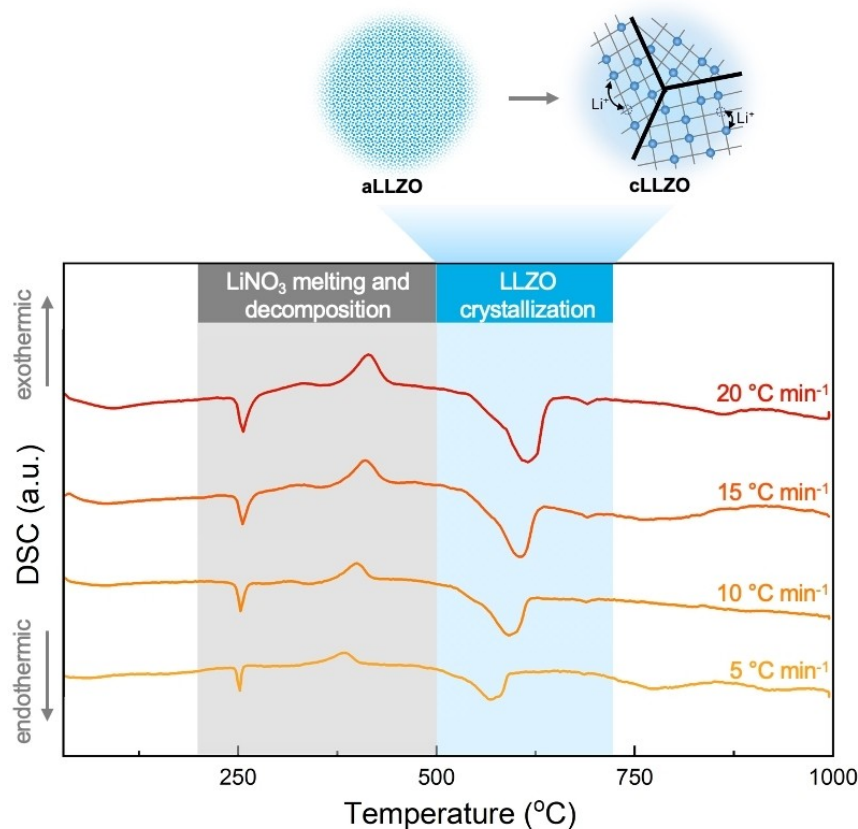
Figure 3. Non-isothermal DSC scans of the LLZO films measured from 25 °C to 1000 °C at four different heating rates of 5, 15, 20, and 25 °C min⁻¹. The two peaks at lower temperatures (shaded in light gray) correspond to melting and decomposition of the LiNO₃ precursor. The two later peaks (shaded in light blue) are considered to be the crystallization peaks for LLZO for further analysis. A schematic illustration of the phase transformation from aLLZO to cLLZO is presented.

the enthalpy consumed at a specific temperature by the sum of the measured enthalpies of the 1st, 2nd, and 3rd crystallization steps. Specifically, the 1st and 2nd crystallization steps account for over 95 % of the enthalpy consumed during transformation from aLLZO to crystallized cLLZO, and the 3rd crystallization step only accounts for < 5 % of the total crystallization enthalpy. Importantly, we note that the progress of crystallization only indicates the amount of enthalpy (heat) consumed at a specific temperature compared to the total enthalpy required to complete the crystallization and should not be directly correlated to the percentage of cubic phase LLZO in the film. We also note that shifts in the crystallization temperature and the progress of crystallization may be detected when compared with the phase evolution detected via in situ techniques, such as in situ TEM,[42] primarily due to the difference in the sample forms used for the measurements (DSC was performed with scratched-off LLZO films vs. the ultra-thin as-deposited LLZO films, i.e., less than 100 nm, used for the in situ TEM study). This difference can lead to shifts in the enthalpy input per unit heating area and results in temperature shifts as LLZO crystallization progresses. The activation energies of the 1st and 2nd crystallization steps have been calculated via Kissinger equation[47] based on the extrapolated slope from Figure 4c and reported in Figure S3 as 1.82 ± 0.05 and

1.76 ± 0.02 eV, respectively. These values are in line with the activation energy of crystallization and grain growth for other ceramic thin films. An example is $Ce_{0.8}Gd_{0.2}O_{1.9-x}$ film prepared by a similar wet-chemical synthesis route, i.e., spray pyrolysis, which exhibited an activation energy of 1.6 eV.[46]

We have now deconvoluted the three crystallization steps based on DSC measurements and revealed the progress-of-crystallization plot based on crystallization enthalpy analysis. In the next section, we apply this information and construct the first TTT diagram for the transformation from aLLZO to crystalline cLLZO films.

Developing the TTT diagram for LLZO

The TTT diagram provides guidelines on the phase evolution over temperature and time and can be used to perform quantitative analysis on the status of the transformation from aLLZO to crystalline cLLZO. By convention, a TTT diagram plots the temperature along the x-axis and the percentage along the y-axis and contains iso-phase lines that represent 1 %, 50 %, and 99 % transformation at different annealing times and temperatures.[45–47,60,61] We obtained this information for the aLLZO to crystalline
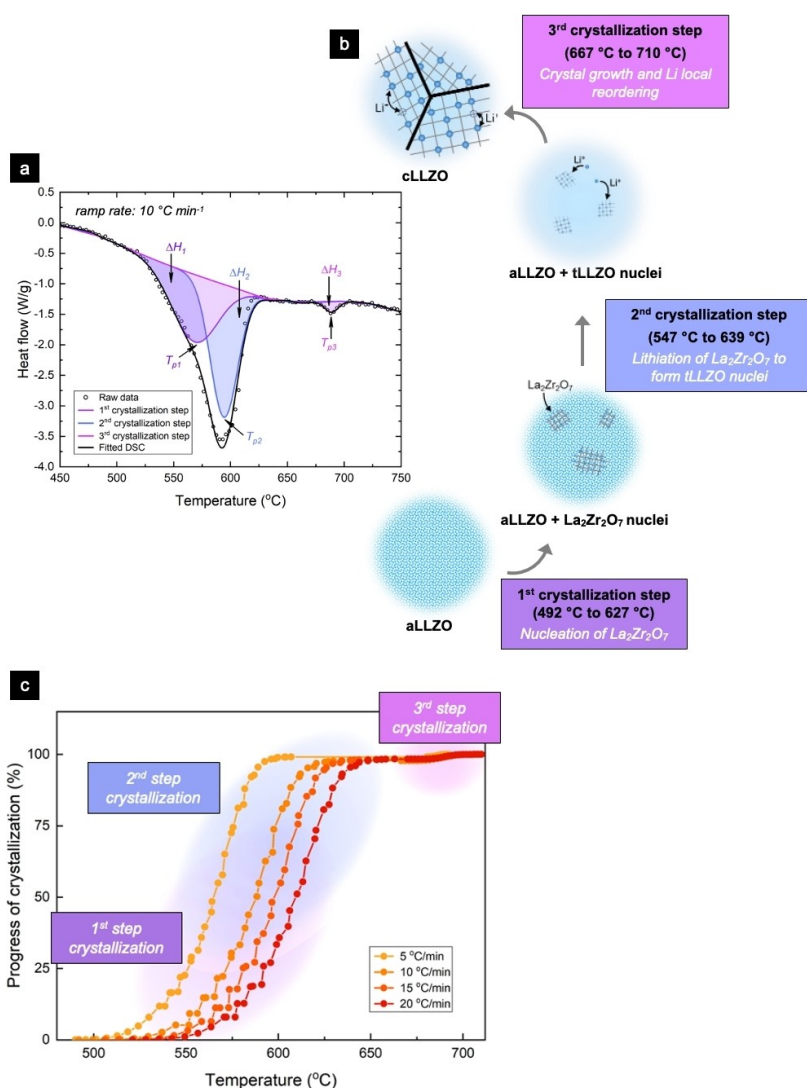
Angew. Chem. Int. Ed. **2023**, *62*, e202304581 (6 of 13)

© 2023 The Authors. Angewandte Chemie International Edition published by Wiley-VCH GmbH

Figure 4. (a) Fitting and deconvolution of the LLZO crystallization peaks for the DSC measured at a heating rate of 10 °C min⁻¹. Two peaks, denoted as the 1ˢᵗ and the 2ⁿᵈ crystallization steps, were deconvolved from the endothermic peak ranges between 492 °C and 639 °C. The minor endothermic peak between 667 °C and 710 °C was identified as the 3ʳᵈ crystallization step. The peak temperature and peak area (enthalpy) for each of the three crystallization steps are indicated in the Figure as T_{p1}, T_{p2}, and T_{p3}, and ΔH_1, ΔH_2, and ΔH_3, repsectively. (b) Schematic illustration of the 1ˢᵗ, 2ⁿᵈ, and 3ʳᵈ crystallization steps. The 1ˢᵗ crystallization step corresponds to the nucleation of $La_2Zr_2O_7$ within the aLLZO matrix. The 2ⁿᵈ crystallization step corresponds to the lithiation and phase transformation from $La_2Zr_2O_7$ to tLLZO. The 3ʳᵈ crystallization step corresponds to the transformation from tLLZO to cLLZO with local Li reordering. (c) Calculated non-isothermal crystallized fraction of LLZO measured at heating rates of 5, 10, 15, and 20 °C min⁻¹. The temperature and transformation fraction ranges corresponding to the 1ˢᵗ, 2ⁿᵈ, 3ʳᵈ crystallization steps are highlighted in violet, lavender blue, and lilac, respectively.

cLLZO transformation from the progress of the transformation plot displayed in Figure 4c and constructed the first TTT diagram for LLZO crystallization in Figure 5.

Specifically, we divide the TTT diagram in two sections: below 480 °C, the film remains amorphous with undecomposed LiNO₃ salt precursor (Ref. [8,42] indicates that LiNO₃ decomposes at 400–480 °C), and above 480 °C, the film undergoes a three-step phase transformation, as detailed in an earlier section, see Figure 4b, from aLLZO to fully crystallized cLLZO. The percentage of transformation data points presented in Figure 5 correspond to specific temperatures and times (as determined for different heating rates in Figure S2b) required to achieve 1%, 25%, 50%, 75%,

and 99% of the transformation from aLLZO to cLLZO. The 1%, 50%, and 99% iso-phase lines represent the beginning, mid-point, and final stage of the transformation, respectively. Specifically, for temperatures above 480 °C and below the 1% iso-phase line, the film is in an amorphous state, i.e., aLLZO, highlighted in light blue. Between the 1% and 99% iso-phase lines, the region in lavender blue represents phase compositions of aLLZO + $La_2Zr_2O_7$ nuclei + tLLZO nuclei, indicating ongoing phase transformations through the 1ˢᵗ and 2ⁿᵈ crystallization steps, see schematic illustration in Figure 5. Finally, we highlight in violet the annealing temperature and time needed to achieve fully crystallized cLLZO for temperatures and times above the
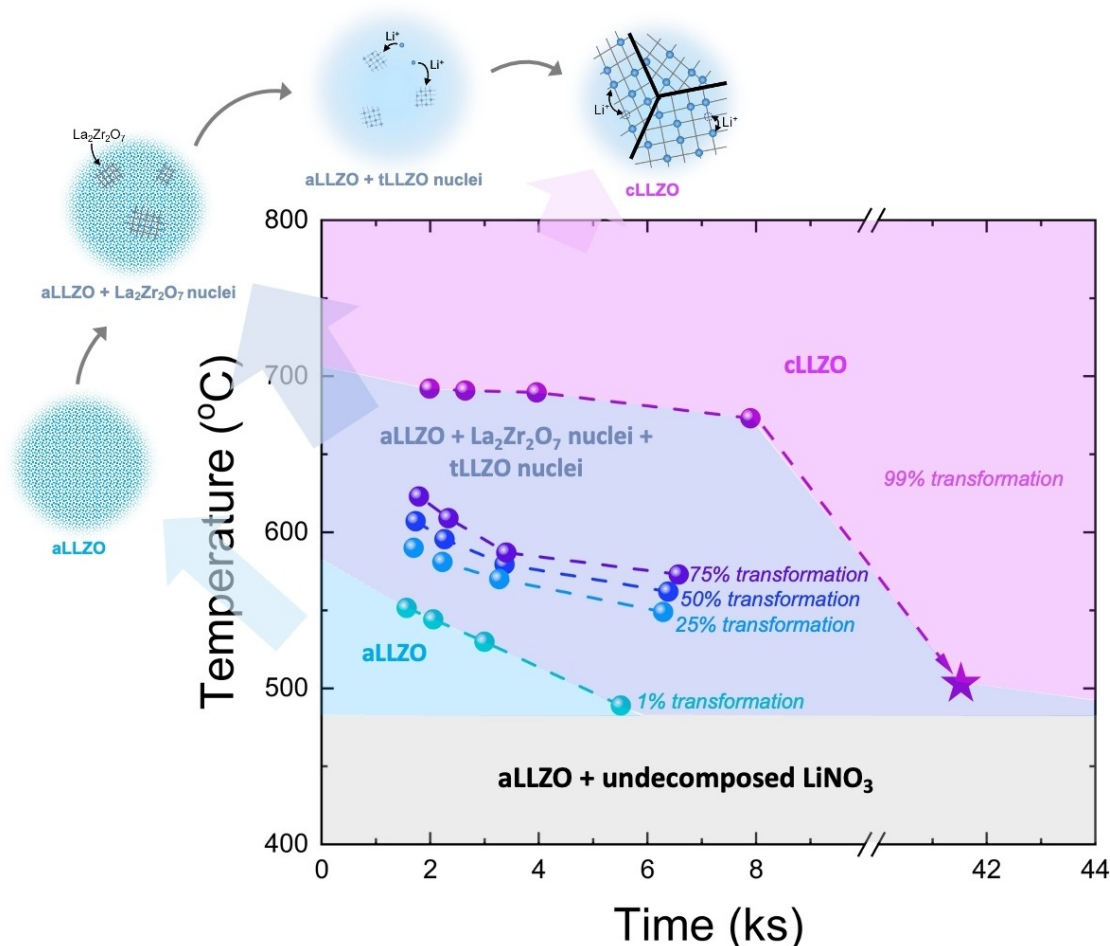
Figure 5. Time-Temperature-Transformation (TTT) diagram for LLZO transforming from the amorphous to crystalline cubic phase. The 1%, 25%, 50%, 75%, and 99% iso-phase lines are presented. Specifically, the 1%, 50% and 99% iso-phase lines are indicated as the beginning, mid-point, and final stage of the phase transformation from amorphous to crystalline cLLZO. The annealing condition of 500°C, 10 h is highlighted. Schematic illustrations of the phase compositions at each crystallization stages are provided. cLLZO, cubic phase LLZO; tLLZO, tetragonal LLZO; aLLZO, amorphous LLZO.

99% transformation iso-phase line. Importantly, we note that the percentage of transformation in the TTT diagram only indicates the ratio of enthalpy consumed at a specific temperature and time to the total enthalpy required to complete the crystallization. This should not be interpreted as the percentage of film that has been transformed into crystalline LLZO phases, as the transformation from aLLZO to cLLZO involves three unique steps, as illustrated in Figure 4b, and requires different enthalpies to complete each step. With extended annealing time, the TTT diagram exhibits a downward trend of annealing temperatures to achieve the same state of phase transformation from aLLZO to crystalline cLLZO. The observed trend suggests that lowering the annealing temperature with extended annealing time may be an alternative route to crystallize LLZO in its cubic phase, as highlighted in Figure 5.

In the next section, we discuss alternative low-temperature processing routes to stabilize cLLZO, as inspired by the TTT diagram, and track their phase and local structure variation via Raman spectroscopy.

Synthesizing cubic-phase LLZO films at reduced temperatures based on TTT diagram phase-evolution roadmap

In the previous section, we demonstrated the successful synthesis of cLLZO at 750°C for 15-min isothermal annealing (denoted as route I) and constructed the TTT diagram for the aLLZO to crystalline cLLZO transformation. Based on the TTT diagram, we propose three alternative post-annealing routes to synthesize cLLZO at lower temperatures and extended isothermal annealing times (Figure 6a). Specifically, these newly defined routes include annealing at 650°C for 5 h (route II), 525°C for 10 h (route III), and 500°C for 10 h (route IV) at an initial heating rate of 5°Cmin^{-1}.

Raman spectroscopy was performed to identify the phase composition and local structure vibration for the LLZO films obtained from the three alternative post-annealing routes, i.e., route II–IV. The three Raman spectra were also compared with the spectrum of cLLZO synthesized via route I, i.e., 750°C for 15-min isothermal annealing,
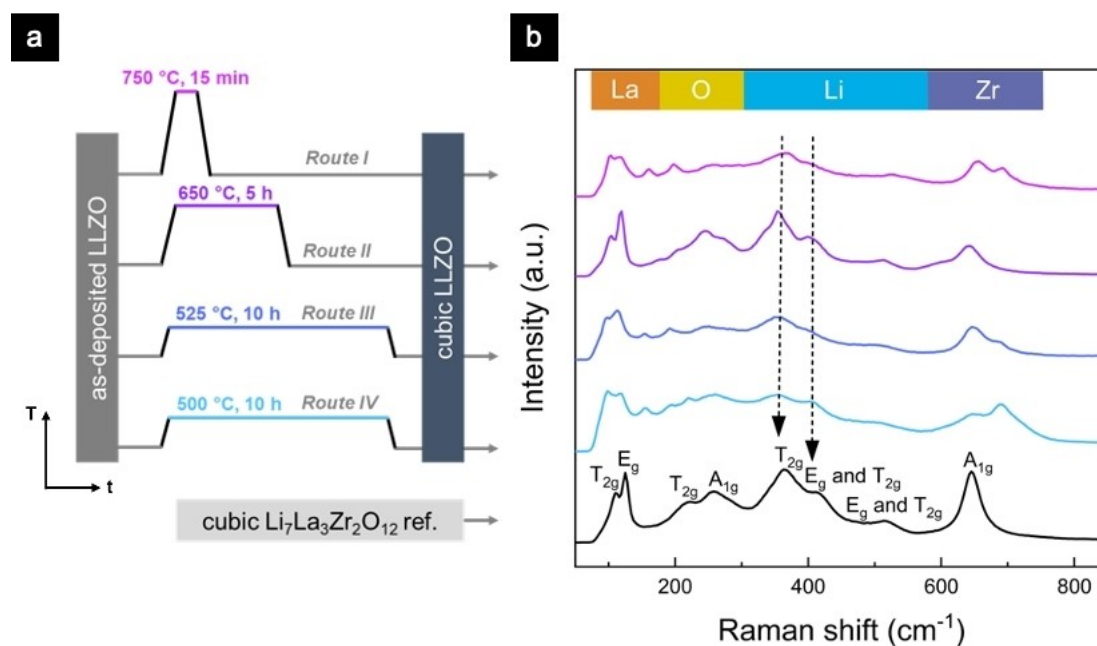
Figure 6. (a) Illustration of the four post-annealing routes (isothermal annealing temperature + isothermal holding time) applied to synthesize cLLZO, including route I of 750 °C for 15 min, route II of 650 °C for 5 h, route III of 525 °C for 10 h, and route IV of 500 °C for 10 h. All four post-annealing routes were performed at a heating rate of 5 °C min^{-1} for both heating and cooling. (b) Raman spectra of the four LLZO films synthesized via post-annealing routes I–IV. Additional reference spectra of cubic Li$_7$La$_3$Zr$_2$O$_{12}$ are displayed in black. All four LLZO films reveal a cubic structure with peak shifts observed for the O–Li–O vibration (352–412 cm^{-1}), suggesting possible variations in structure compaction and local strain among the four cLLZO films.

as displayed in Figure 6b. Overall, the spectra of the four LLZO films all reveal cubic-phase structures but with noticeable shifts of the O–Li–O vibration bands and peak divergence of the O–Zr–O stretching band.

We first summarize the Raman peaks observed in the four LLZO spectra. The two intense peaks at 94 and 113 cm^{-1} were identified as the T$_{2g}$ and E$_g$ modes of O–La–O vibration, and the peaks centered at 220 and 265 cm^{-1} were assigned to the oxygen-bending band of T$_{2g}$ and A$_{1g}$, respectively.[50] The pronounced peaks centered at 360 and 404 cm^{-1} and the minor peak centered at 514 cm^{-1} were attributed to the O–Li–O vibration bands (E$_g$ and T$_{2g}$) in LiO$_6$ octahedra,[51] and the two peaks at 651 and 686 cm^{-1} correspond to the O–Zr–O stretching band (A$_{1g}$ mode). In addition to the major Raman peaks in the four spectra corresponding to cubic phase LLZO, we also observed minor peaks at 160 and 198 cm^{-1} in all the spectra, attributable to the rotatory and translator motion of CO$_3^{2-}$ from the surface chemistry variation of Li$_2$CO$_3$.[56,57]

We next performed detailed analysis on the O–Li–O and O–Zr–O bands, as Li and Zr are the two network formers that define the local structure and transformation from aLLZO to crystalline cLLZO. Additionally, the Li–O bond length can affect the activation energy needed for Li to hop from one site to another, which is a critical property in determining its use in solid-state batteries. To understand how different annealing routes affect the local structures and bonding around Li, we fitted the two major O–Li–O vibrational bands (E$_g$ and T$_{2g}$) and reported their fitted positions in Figure S3. Upon lowering the annealing temper-

ature from 750 °C to 650 °C (and therefore prolonging the annealing time), the E$_g$ and T$_{2g}$ peaks first exhibited redshifts from 368 to 354 cm^{-1} and from 407 to 401 cm^{-1}, respectively. Further lowering the annealing temperature to 500 °C led to a blueshift of the E$_g$ and T$_{2g}$ peak to 410 cm^{-1} with no change of the T$_{2g}$ peak position near 354 cm^{-1}. In general, a redshift of the Raman peaks suggests longer bond lengths (and vice versa for a blueshift). The observed trend indicates a longer Li–O bond in LiO$_6$ octahedra when annealed at 650 °C for 5 h as compared to those annealed at 500 °C, 525 °C, and 750 °C. In general, a longer Li–O bond suggests a lower bond strength and therefore reduced energy required for Li$^+$ to migrate to its neighboring sites, which is preferred for application as a solid electrolyte or protective coating layer in batteries.[62–64]

We also observed peak divergence of the O–Zr–O stretching band (A$_{1g}$ mode) with two peaks emerging at various ratios at 651 and 686 cm^{-1} for films annealed at different temperatures and times.[50,51] The appearance of the two peaks may be defect-related or may be correlated to the co-existence of two LLZO cubic phases (i.e., 220 and 230 space-group cLLZO), introducing anisotropic strains to the lattice (as detailed in the earlier Raman section).[52,53]

In summary, all four annealing routes with isothermal temperatures ranging between 500 and 750 °C resulted in successful synthesis of cLLZO films. We observed two interesting phenomena from the collected Raman spectra, including: *i.* significant O–Li–O vibrational bands shifts and *ii.* O–Zr–O stretching band divergence for LLZO films crystallized at different temperatures. Similar O–Li–O

vibrational band shifts have been reported in previous studies on PLD-processed aLLZO and cLLZO films, with the shifts attributed to variations in the Li$^+$ concentration (lithiation) and the small LLZO nanocrystallite sizes.[24] Indeed, these may also be the reasons leading to the O–Li–O vibrational band shifts in the current study, as different isothermal temperatures can result in different nucleation rates, affecting the size of the LLZO nanocrystallite and local strains. Furthermore, variation in the annealing time and temperature may also lead to different amounts of Li losses (that is, different Li concentrations remain in the LLZO films), therefore affecting the ratio of the 220 and 230 space-group cubic grains and generating anisotropic local strains in polycrystalline cLLZO films. Further investigation using experimental and computational methods (e.g., DFT and high-energy X-ray spectroscopies) is required to understand the origin of the A$_{1g}$ peak divergence of the O–Zr–O stretching band and to clarify the role of the annealing temperature and time on the distribution of grain sizes and cubic-phase compositions (i.e., 220 vs. 230 space groups), as they may have substantial implications on the Li-ion dynamics for solid-state battery applications.[10,12]

Advantages of low-temperature annealed LLZO films

We compared, from cost and battery integration perspectives, the processing temperatures and times required to achieve cLLZO, as proposed in this study, i.e., route I–IV, to those reported in the literature for bulk-type pellets/tapes and thin-film LLZO in Figure 7. Here, we only note the maximum annealing/sintering temperatures and the corresponding isothermal time, as these factors play a key role in determining the stability at LLZO-cathode interfaces during co-processing and defining the thermal budget and associated processing costs. Importantly, we highlight the newly proposed processing routes with annealing temperatures of 500 °C and 525 °C, representing the lowest annealing temperatures reported to crystallize LLZO films. These temperatures are particularly attractive for reducing interfacial degradation during LLZO-cathode co-processing.
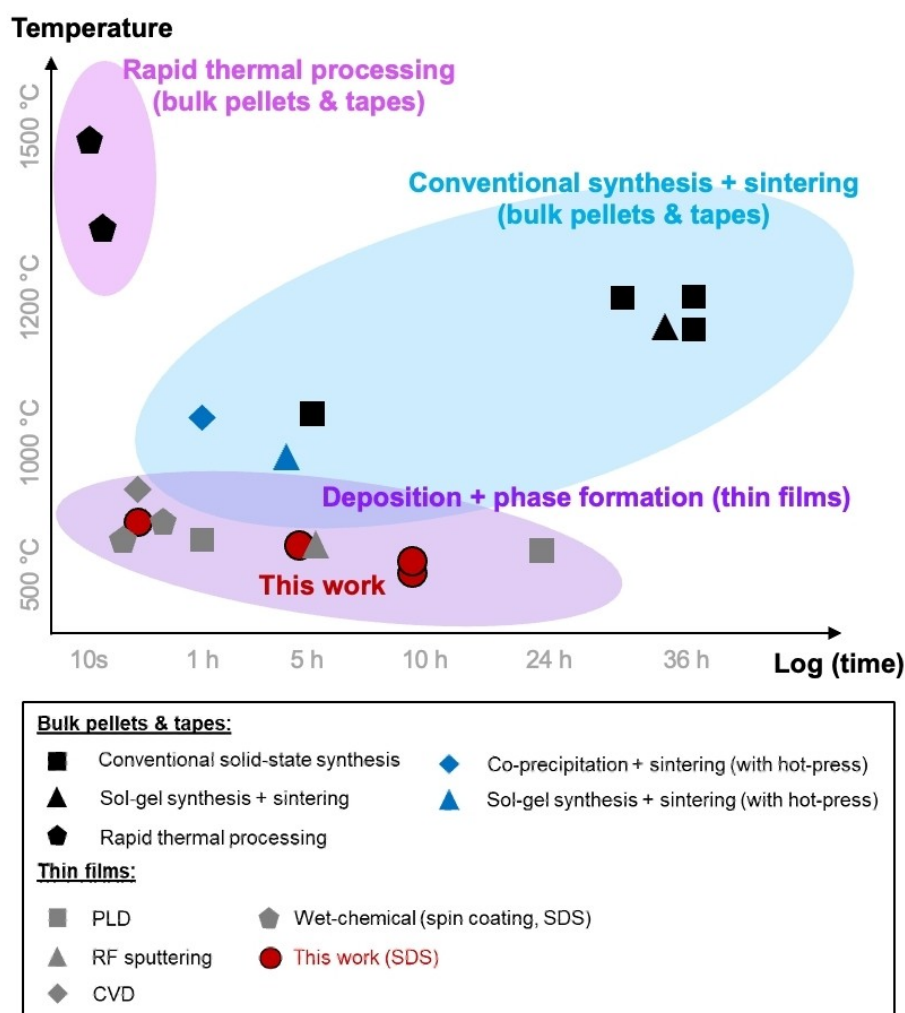

Figure 7. Comparison of the maximum processing temperature and processing time of bulk[21,25–32] (pellets and tapes) and thin-film[8,24,34–37] LLZO via different synthesis routes.

Specifically, we outline in Figure 7 the three major routes to process cLLZO, namely, conventional synthesis + sintering for bulk pellets and tapes (highlighted in light blue), rapid thermal processing for bulk pellets and tapes (highlighted in lilac), and deposition + phase formation for thin films (highlighted in violet) and provide a brief discussion on their maximum sintering or annealing temperature and time as follows. The bulk pellet and tapes processed via conventional synthesis + sintering generally require a high-temperature sintering process at 1050–1230 °C for 1–36 h (generally > 5 h) to eliminate pores and achieve complete densification.[21,25–27] There are a few variations of the conventional synthesis + sintering routes for which the LLZO powder (starting material for LLZO pellet sintering) may be synthesized via different routes, including sol-gel synthesis + sintering[30,31] and co-precipitation + sintering;[32] hot pressing may also be used to facilitate densification during these processes.[31,32] However, this method is not cost-effective for LLZO-cathode co-processing because of the high sintering temperature and long sintering time. Alternatively, we consider rapid thermal processing as a more cost-effective route for sintering bulk pellets and tapes, which generally requires a sintering temperature of > 1300 °C for 10–15 s.[28,29] However, the thicknesses that can be achieved via bulk pellet/tape sintering (i.e., < 25 μm) are not of particular interest toward battery integration as they will unavoidably increase the internal resistance and lower the energy density of the cell.

To further enhance the energy density, thin-film LLZO with a thickness < 10 μm is preferred.[1] Thin-film LLZO can be deposited using vacuum-based or wet-chemical methods and then annealed at a much lower temperature to transform the film from the amorphous to crystalline cubic phase without the need for sintering to achieve densification. The annealing temperature for thin-film LLZO typically ranges between 600 and 950 °C with an isothermal time of 15 min to 24 h.[8,24,34–38] More excitingly, our newly designed annealing method enables the synthesis of cLLZO films using a direct liquid-to-solid method at temperatures as low as 500 °C (for 10-h isothermal annealing), which is a significantly lower temperature than that used in previously reported methods. Admittedly, there is still room to further shorten the isothermal time for the 500 °C annealing route to promote its direct integration with the state-of-the-art roll-to-roll processes for battery cells. Future work is recommended to focus on exploring the crystallization kinetics for LLZO with various dopants and optimized Li+ concentrations to further reduce the processing time needed to crystallize cLLZO.

In summary, solid-state electrolyte films are essential components in future high-energy solid-state batteries to enable direct pairing with a Li-metal anode and high-voltage cathodes. The newly developed low-temperature annealing routes for cLLZO synthesis shed light on LLZO-cathode co-processing strategies without the need for sintering, providing room to further boost the energy and power densities of the cell at a reduced cost.

Conclusion

Novel lower-energy- and cost-intensive functional ceramic synthesis routes are essential to define socio-economically tolerable solid Li+-conductive electrolytes for all-solid-state and hybrid batteries. The Li-garnet-type solid-state electrolytes offer a promising option for achieving these goals owing to their high room-temperature Li+ conductivity up to 10^{-4} S cm^{-1} and wide electrochemical stability window (i.e., 0–6 V) that enables stable pairing with Li metal and high-voltage cathodes. Despite the promise, the scale-up fabrication for these functional Li-containing ceramics has been hindered by their limited chemical stability toward co-processing and integration with Co-reduced cathodes, such as NMC and NCA, at a temperature above 600 °C. The high processing costs associated with ceramic powder processing and high-temperature sintering is another obstacle limiting their scale-up, especially during energy price spikes, as experienced in 2022. Therefore, there is a need for the solid-state battery and glass-ceramic industries to redefine the ceramic processing routes, such as for cLLZO solid electrolytes, toward lower temperatures with a possible reduction of sintering steps.

In this work, we provide evidence and alternative routes to synthesize cLLZO films via SDS, a "liquid-to-solid" direct densification method, to aid the integration of LLZO electrolyte separators in solid-state batteries at approximately half of the classic sintering temperatures that are typically used to densify cLLZO pellets and tapes. We developed through this work the very first TTT diagram for the glass-ceramic LLZO material based on a crystallization enthalpy analysis as well as local structure and phase evolution studies. This is an important step, as we demonstrated in prior work, see Refs. [8,42], that LLZO can be synthesized and fully densified through an amorphous-to-crystalline cubic multi-step phase transformation at 750 °C. Nevertheless, the optimal heating rate and minimum crystallization temperature to reach the fast-conducting cubic phase remained unclear. The TTT diagram established for the Li+ solid-electrolyte cLLZO provides insights on optimizing the synthesis conditions to achieve the lowest crystallization temperature ever reported to stabilize cLLZO as a dense solid film at 500 °C with 10-h isothermal annealing, as proven through Raman spectroscopy in this work. Looking ahead, we see a bright future for the use of direct liquid-to-solid densification synthesis routes such as SDS synthesis in a combination with TTT diagram analysis to define new processing routes for low costs and sustainable battery production.

Contributions

Y.Z. and J.L.M.R. proposed the TTT model of the study. Y.Z. designed the experiments and performed the data analysis. Y.Z. and J.L.M.R. wrote and discussed the manuscript with the help of all the coauthors.

Acknowledgements

Conflict of Interest

The authors declare no conflict of interest.

Data Availability Statement

The data that support the findings of this study are available from the corresponding author upon reasonable request.

Keywords: Ceramics · LLZO · Li Garnets · Solid-State Electrolytes · Time-Temperature-Transformation Diagram

[1] M. Balaish, J. C. Gonzalez-Rosillo, K. J. Kim, Y. Zhu, Z. D. Hood, J. L. M. Rupp, *Nat. Energy* **2021**, *6*, 227–239.

[2] Y. Ding, Z. P. Cano, A. Yu, J. Lu, Z. Chen, *Electrochem. Energy Rev.* **2019**, *2*, 1–28.

[3] R. Schmuch, R. Wagner, G. Horpel, T. Placke, M. Winter, *Nat. Energy* **2018**, *3*, 267–278.

[4] X. G. Yang, T. Liu, C. Y. Wang, *Nat. Energy* **2021**, *6*, 176–185.

[5] G. Bhutada, "Breaking Down the Cost of an EV Battery Cell," can be found under https://www.visualcapitalist.com/breaking-down-the-cost-of-an-ev-battery-cell/, **2022**.

[6] *National Blueprint for Lithium Batteries 2021–2030*, **2021**.

[7] K. J. Kim, M. Balaish, M. Wadaguchi, L. Kong, J. L. M. Rupp, *Adv. Energy Mater.* **2021**, *11*, 2002689.

[8] Z. D. Hood, Y. Zhu, L. J. Miara, W. S. Chang, P. Simons, J. L. M. Rupp, *Energy Environ. Sci.* **2022**, *15*, 2927–2936.

[9] S. Kalnaus, A. S. Westover, M. Kornbluth, E. Herbert, N. J. Dudney, *J. Mater. Res.* **2021**, *36*, 787–796.

[10] Y. Zhu, M. Balaish, J. L. M. Rupp, *Joule* **2022**, *6*, 2680–2682.

[11] J. H. Cho, K. Kim, S. Chakravarthy, X. Xiao, J. L. M. Rupp, B. W. Sheldon, *Adv. Energy Mater.* **2022**, *12*, 2200369.

[12] M. B. Dixit, B. S. Vishugopi, W. Zaman, P. Kenesei, J. S. Park, J. Almer, P. P. Mukherjee, K. B. Hatzell, *Nat. Mater.* **2022**, *21*, 1298–1305.

[13] H. J. Deiseroth, S. T. Kong, H. Eckert, J. Vannahme, C. Reiner, T. Zaiß, M. Schlosser, *Angew. Chem. Int. Ed.* **2008**, *47*, 755–758.

[14] S. Boulineau, M. Courty, J. M. Tarascon, V. Viallet, *Solid State Ionics* **2012**, *221*, 1–5.

[15] F. Mizuno, A. Hayashi, K. Tadanaga, M. Tatsumisago, *Adv. Mater.* **2005**, *17*, 918–921.

[16] H. Xu, Y. Yu, Z. Wang, G. Shao, *Energy Environ. Mater.* **2019**, *2*, 234–250.

[17] Y. Zhu, X. He, Y. Mo, *J. Mater. Chem. A* **2016**, *4*, 3253–3266.

[18] Y. Zhu, J. C. Gonzalez-Rosillo, M. Balaish, Z. D. Hood, K. J. Kim, J. L. M. Rupp, *Nat. Rev. Mater.* **2021**, *6*, 313–331.

[19] J. Li, C. Ma, M. Chi, C. Liang, N. J. Dudney, *Adv. Energy Mater.* **2015**, *5*, 1401408.

[20] R. Murugan, V. Thangadurai, W. Weppner, *Angew. Chem. Int. Ed.* **2007**, *46*, 7778–7781.

[21] E. Yi, H. Shen, S. Heywood, J. Alvarado, D. Y. Parkinson, G. Chen, S. W. Sofie, M. M. Doeff, *ACS Appl Energy Mater* **2020**, *3*, DOI 10.1021/acsaem.9b02101.

[22] E. J. Cheng, M. Liu, Y. Li, T. Abe, K. Kanamura, *J. Power Sources* **2022**, *517*, 230705.

[23] R. Pfenninger, M. Struzik, I. Garbayo, E. Stilp, J. L. M. Rupp, *Nat. Energy* **2019**, *4*, 475–483.

[24] K. J. Kim, J. L. M. Rupp, *Energy Environ. Sci.* **2020**, *13*, 4930–4945.

[25] H. Buschmann, J. Dölle, S. Berendts, A. Kuhn, P. Bottke, M. Wilkening, P. Heitjans, A. Senyshyn, H. Ehrenberg, A. Lotnyk, V. Duppel, L. Kienle, J. Janek, *Phys. Chem. Chem. Phys.* **2011**, *13*, 19378–19392.

[26] S. Ohta, T. Kobayashi, T. Asaoka, *J. Power Sources* **2011**, *196*, 3342–3345.

[27] C. Wang, W. Ping, Q. Bai, H. Cui, R. Hensleigh, R. Wang, A. H. Brozena, Z. Xu, J. Dai, Y. Pei, C. Zheng, G. Pastel, J. Gao, X. Wang, H. Wang, J. C. Zhao, B. Yang, X. Zheng, J. Luo, Y. Mo, B. Dunn, L. Hu, *Science* **2020**, *368*, 521–526.

[28] T. Clemenceau, N. Andriamady, P. Kumar, M. K. A. Badran, V. Avila, K. Dahl, M. Hopkins, X. Vendrell, D. Marshall, R. Raj, *Scr. Mater.* **2019**, *172*, 1–5.

[29] Y. Li, J. T. Han, C. A. Wang, S. C. Vogel, H. Xie, M. Xu, J. B. Goodenough, *J. Power Sources* **2012**, *209*, 278–281.

[30] J. Sakamoto, E. Rangasamy, H. Kim, Y. Kim, J. Wolfenstine, *Nanotechnology* **2013**, *24*, 424005.

[31] J. L. Allen, J. Wolfenstine, E. Rangasamy, J. Sakamoto, *J. Power Sources* **2012**, *206*, 315–319.

[32] S. Afyon, F. Krumeich, J. L. M. Rupp, *J. Mater. Chem. A* **2015**, *3*, 18636–18648.

[33] M. Rawlence, I. Garbayo, S. Buecheler, J. L. M. Rupp, *Nanoscale* **2016**, *8*, 14746–14753.

[34] M. Rawlence, A. N. Filippin, A. Wäckerlin, T. Y. Lin, E. Cuervo-Reyes, A. Remhof, C. Battaglia, J. L. M. Rupp, S. Buecheler, *ACS Appl. Mater. Interfaces* **2018**, *10*, 13720–13728.

[35] R. J. Chen, M. Huang, W. Z. Huang, Y. Shen, Y. H. Lin, C. W. Nan, *J. Mater. Chem. A* **2014**, *2*, 13277–13282.

[36] H. Katsui, T. Goto, *Thin Solid Films* **2015**, *584*, 130–134.

[37] K. Tadanaga, H. Egawa, A. Hayashi, M. Tatsumisago, J. Mosa, M. Aparicio, A. Duran, *J. Power Sources* **2015**, *273*, 844–847.

[38] R. Mahbub, K. Huang, Z. Jensen, Z. D. Hood, J. L. M. Rupp, E. A. Olivetti, *Electrochem. Commun.* **2020**, *121*, 106860.

[39] L. Miara, A. Windmüller, C. L. Tsai, W. D. Richards, Q. Ma, S. Uhlenbruck, O. Guillon, G. Ceder, *ACS Appl. Mater. Interfaces* **2016**, *8*, 26842–26850.

[40] C. Bauer, S. Burkhardt, N. P. Dasgupta, L. A. W. Ellingsen, L. L. Gaines, H. Hao, R. Hischier, L. Hu, Y. Huang, J. Janek, C. Liang, H. Li, J. Li, Y. Li, Y. C. Lu, W. Luo, L. F. Nazar, E. A. Olivetti, J. F. Peters, J. L. M. Rupp, M. Weil, J. F. Whitacre, S. Xu, *Nat. Sustainability* **2022**, *5*, 176–178.

[41] Y. Zhu, Z. D. Hood, H. Paik, P. B. Groszewicz, S. P. Emge, F. N. Sayed, C. Sun, M. Balaish, D. Ehre, L. J. Miara, A. Frenkel, I. Lubomirsky, C. P. Grey, J. L. M. Rupp, *Under review* **2022**.

[42] C. B. Carter, M. G. Norton, in *Ceramic Materials*, Springer, Berlin, Heidelberg, **2013**, pp. 457–475.

[43] D. R. Uhlmann, *J. Non-Cryst. Solids* **1980**, *38*, 693–698.

[44] M. C. Weinberg, D. P. Birnie, V. A. Shneidman, *J. Non-Cryst. Solids* **1997**, *219*, 89–99.

[45] J. L. M. Rupp, B. Scherrer, N. Schauble, L. J. Gauckler, *Adv. Funct. Mater.* **2010**, *20*, 2807–2814.

[46] H. E. Kissinger, *Anal. Chem.* **1957**, *29*, 1702–1706.

[47] G. F. vander Voort, *Atlas of Time-Temperature Diagrams for Irons and Steels*, **1991**.

[48] Y. Zhu, W. S. Chang, L. Miara, J. L. M. Rupp, *Lithium Solid Electrolyte and Method of Manufacture Thereof* **2019**, 16/860,326, https://patentimages.storage.googleapis.com/d8/fb/e2/b4b4d535ef55a2/US11757127.pdf.

[49] G. Larraz, A. Orera, M. L. Sanjuán, *J. Mater. Chem. A* **2013**, *1*, 11419–11428.

[50] F. Tietz, T. Wegener, M. T. Gerhards, M. Giarola, G. Mariotto, *Solid State Ionics* **2013**, *230*, 77–82.

[51] R. Schmitt, A. Nenning, O. Kraynis, R. Korobko, A. I. Frenkel, I. Lubomirsky, S. M. Haile, J. L. M. Rupp, *Chem. Soc. Rev.* **2020**, *49*, 554–592.

[52] Y. U. Shi, A. H. Bork, S. Schweiger, J. L. M. Rupp, *Nat. Mater.* **2015**, *14*, 721–727.

[53] B. P. Mandal, P. S. R. Krishna, A. K. Tyagi, *J. Solid State Chem.* **2010**, *183*, 41–45.

[54] B. E. Scheetz, W. B. White, *J. Am. Ceram. Soc.* **1979**, *62*, 468–470.

[55] M. H. Brooker, J. Wang, *Spectrochim. Acta Part A* **1992**, *48*, 999–1008.

[56] Y. Hase, I. V. P. Yoshida, *Monatsh. Chem.* **1980**, *111*, 1265–1272.

[57] N. Bernstein, M. D. Johannes, K. Hoang, *Phys. Rev. Lett.* **2012**, *109*, 205702.

[58] M. Zhao, L. Zou, Y. Wu, *Energy Procedia* **2017**, *143*, 792–797.

[59] C. Chattopadhyay, A. Prasad, B. S. Murty, *Acta Mater.* **2018**, *153*, 214–225.

[60] M. S. Zarabad, M. Rezvani, *Results Phys.* **2018**, *10*, 356–359.

[61] C. A. Geiger, E. Alekseev, B. Lazic, M. Fisch, T. Armbruster, R. Langner, M. Fechtelkord, N. Kim, T. Pettke, W. Weppner, *Inorg. Chem.* **2011**, *50*, 1089–1097.

[62] J. Ziolkowski, *J. Solid State Chem.* **1985**, *57*, 269–290.

[63] I. D. Brown, R. D. Shannon, *Acta Crystallogr. Sect. A* **1973**, *29*, 266–282.

[64] I. Garbayo, M. Struzik, W. J. Bowman, R. Pfenninger, E. Stilp, J. L. M. Rupp, *Adv. Energy Mater.* **2018**, *8*, 1702265.